

PAPER • OPEN ACCESS

Phonon spectra of pure and acceptor doped BaZrO₃ investigated with visible and UV Raman spectroscopy




To cite this article: Laura Mazzei *et al* 2020 *J. Phys.: Condens. Matter* **32** 405403

View the [article online](#) for updates and enhancements.

You may also like

- [Photoluminescence Characterization of Defects in Rapidly Annealed Ultra Shallow Junctions](#)
Masahiro Yoshimoto, Masashi Okutani, Gota Murai et al.
- [Understanding the growth mechanism of BaZrS₃ chalcogenide perovskite thin films from sulfurized oxide precursors](#)
Santhanu Panikar Ramanandan, Andrea Giunto, Elias Z Stutz et al.
- [A DFT study of structural, electronic and optical properties of pristine and intrinsic vacancy defects containing barium zirconate \(BaZrO₃\) using mBJ potential](#)
Nazia Erum, Muhammad Azhar Iqbal and Imran Bashir

Phonon spectra of pure and acceptor doped BaZrO₃ investigated with visible and UV Raman spectroscopy

Laura Mazzei^{1,2} , Dieter Rukser³, Florian Biebl³ , Benjamin Grimm-Lebsanft³, Gerd Neuber³, Daniele Pergolesi⁴, Lars Börjesson¹, Michael A Rübhausen³, Jakob Andreasson^{1,5} and Maths Karlsson^{2,6} 

¹ Department of Physics, Chalmers University of Technology, 412 96 Göteborg, Sweden

² Department of Chemistry and Chemical Engineering, Chalmers University of Technology, 412 96 Göteborg, Sweden

³ Institut für Nanostruktur- und Festkörperphysik, Universität Hamburg, Center for Free Electron Laser Science (CFEL), Luruper Chaussee 149, 22761 Hamburg, Germany

⁴ Laboratory for Multiscale Materials Experiments, Paul Scherrer Institute, 5232 Villigen-PSI, Switzerland

⁵ ELI Beamlines, Institute of Physics of the Czech Academy of Sciences, Na Slovance 2, 182 21, Prague, Czech Republic

E-mail: maths.karlsson@chalmers.se

Received 17 March 2020, revised 13 May 2020

Accepted for publication 22 May 2020

Published 1 July 2020



Abstract

We report results from visible and UV Raman spectroscopy studies of the phonon spectra of a polycrystalline sample of the prototypical perovskite type oxide BaZrO₃ and a 500 nm thick film of its Y-doped, proton conducting, counterpart BaZr_{0.8}Y_{0.2}O_{2.9}. Analysis of the Raman spectra measured using different excitation energies (between 3.44 eV and 5.17 eV) reveals the activation of strong resonance Raman effects involving all lattice vibrational modes. Specifically, two characteristic energies were identified for BaZrO₃, one around 5 eV and one at higher energy, respectively, and one for BaZr_{0.8}Y_{0.2}O_{2.9}, above 5 eV. Apart from the large difference in spectral intensity between the non-resonant and resonant conditions, the spectra are overall similar to each other, suggesting that the vibrational spectra of the perovskites are stable when investigated using an UV laser as excitation source. These results encourage further use of UV Raman spectroscopy as a novel approach for the study of lattice vibrational dynamics and local structure in proton conducting perovskites, and open up for, e.g., time-resolved experiments on thin films targeted at understanding the role of lattice vibrations in proton transport in these kinds of materials.

Keywords: proton, oxide, resonance, Raman, vibration

 Supplementary material for this article is available [online](#)

(Some figures may appear in colour only in the online journal)

⁶ Author to whom any correspondence should be addressed.



Original content from this work may be used under the terms of the [Creative Commons Attribution 4.0 licence](#).

Any further distribution of this work must maintain attribution to the author(s) and the title of the work, journal citation and DOI.

1. Introduction

Acceptor-doped perovskite type oxides, such as Y-doped BaZrO₃ (BZO), are currently receiving considerable attention because of their proton conducting properties and concomitant potential as electrolytes for hydrogen fuel cells and gas separation membranes [1]. In the hydrated form of these materials, the protons are bonded as O–H groups where the H is hydrogen-bonded to a neighboring oxygen, O–H ··· O. On a local scale, the protons can diffuse through a repetition of proton transfers (jumps) from a specific oxygen atom to another one, and an intermediate reorientational motion of the O–H group between such transfers [2]. Crucially, the ability of the protons to diffuse depends strongly on the vibrational dynamics of the system. For example, the localized vibrational modes of protons, i.e. O–H stretching and O–H wagging (bending) modes, are known to affect the proton transfer and O–H reorientational motions [2, 3] and furthermore, the dynamics of the oxygen atoms play an important role as they influence the proton jump distance [2, 4, 5]. Vibrationally assisted proton transfer in oxides has been suggested both by theoretical analysis [6–8] and by time-resolved vibrational spectroscopy experiments [9, 10].

A new possibility to advance further the understanding of the relationship between structural and dynamical properties in proton conducting oxides is given by studies of samples in the form of (thin) films. This is because with film samples one can manipulate the degree of crystallinity and introduce strain and distortions in the structure, offering new opportunities for studies of structure and dynamics using, e.g., vibrational spectroscopy. Furthermore, by using films, it is possible to effectively remove grain-boundary effects, a well-known obstacle for proton conduction [11–13]. By inducing lattice strain, the proton conducting properties can be improved even further [14, 15]. Additionally, there is a growing interest in miniaturized power generation devices based on thin films of proton conducting oxides, which could be used for mobile applications, such as portable electronic devices, and potentially allow a lowering of operation temperatures [16, 17].

With regard to vibrational spectroscopy, it would thus be of great interest to study thin film samples of proton conductors, both with Raman and infrared (IR) spectroscopy, as well as with time-resolved (pump-probe) techniques. However, compared to vibrational spectroscopy experiments on bulk samples [18–25], the study of thin film samples may be challenging, because of the heavily reduced sample volume and concomitantly low Raman scattering, or IR absorbance, signal. Additionally, films of acceptor-doped BZO are essentially transparent to visible light [26–28] and the depth resolution of the light is generally in the range of ≈ 400 –700 nm, i.e. of the order of its wavelength. For the case of Raman spectroscopy, this implies that studies of samples such as a thin film on a substrate is often difficult because of a strong background signal from the underlying substrate material that overwhelms the weaker signal from the sample. Using ultraviolet (UV) light would potentially reduce such an unwanted background signal in Raman spectroscopy experiments. This is because UV light has a smaller depth resolution and perovskite type oxides

are not generally transparent to UV light as they are to visible light [26–28]. Further, UV Raman spectroscopy may allow measurements under resonant conditions, i.e. when the excitation energy is tuned to overlap with (or be very close to) an electronic transition of the material. In such a case, the overall intensity of the Raman scattering signal from the sample can be greatly enhanced and/or altered.

Here, we report on a study of the vibrational spectra of BZO based oxides performed by means of both visible and UV Raman spectroscopy, with excitation energies of 2.41 eV (514 nm wavelength), and between 2.95 eV and 5.17 eV (420–240 nm wavelength), respectively. The aim of the study is to compare the Raman spectra measured for different excitation energies, identify potential resonant energies, and to determine the key aspects of UV/resonant Raman spectroscopy applied to perovskite type oxides. For this purpose, two different types of samples were used, a large polycrystalline sample of BZO, approximately $2 \times 2 \times 5$ mm³, and a 500 nm thick film of 20% Y-doped BZO (BaZr_{0.8}Y_{0.2}O_{2.9}, 20Y/BZO). The large polycrystalline BZO sample is suitable for both visible and UV Raman spectroscopy measurements and thus allows a comparison between these techniques. On the contrary, the 20Y/BZO film is a challenging sample for visible Raman spectroscopy, because of the much smaller sample volume, coupled with the high transparency to visible light. However, our results show that with the use of UV Raman spectroscopy, the signal can be significantly enhanced, exactly as expected. Furthermore, we show that the two techniques provide very similar vibrational information. The implications of these results are discussed in view of the key benefits and prospect of UV Raman spectroscopy for studies of pure and acceptor-doped perovskite materials.

2. Experimental details

2.1. Sample preparation

The 500 nm thick film of 20Y/BZO was grown by pulsed laser deposition (PLD) on a (100)-oriented MgO substrate (10 mm \times 5 mm \times 0.5 mm) using a KrF excimer laser (Coherent Lambda Physik GmbH) with a wavelength of 248 nm and a pulse width of 25 ns. A dense 20Y/BZO pellet was used as target for the deposition, and the target-to-substrate distance was set to 5 cm. An oxygen partial pressure of 0.1 mbar, a laser fluence of about 2 J cm^{−2} and a laser repetition rate of 10 Hz were used during the deposition. The deposition temperature, monitored with a pyrometer, was set at about 750 °C. To ensure good thermal contact with the heating plate and accurate temperature reading, silver paste was applied between the heating plate and the substrate.

The use of (100)-oriented MgO as substrate material is motivated by the excellent lattice matching between the cubic perovskite structure of Y-doped BZO (≈ 4.22 Å) [11, 13, 14] and the cubic rock-salt structure of MgO (4.21 Å). This allows minimizing lattice strain at the film/substrate interface. The substrate was ultrasonically cleaned in acetone and isopropanol before the deposition.

The polycrystalline sample of BZO was prepared by induction skull-melting, as described in reference [29].

2.2. Raman spectroscopy

Raman spectroscopy using light with an incident wavelength of 514 nm (2.41 eV) was performed on the polycrystalline BZO sample. The Raman spectrum (150–1300 cm^{-1}) was measured on a Dilor XY-800 triple-grating spectrometer equipped with an Ar^+/Kr^+ laser. The laser was focused, with a circular beam size of approximately 0.8 μm in diameter and a power of 3 mW, on the sample through a $\times 50$ objective lens under an optical microscope. The dispersed light was recorded by a CCD detector cooled with liquid nitrogen. Measurements on the 20Y/BZO film were also attempted under the same conditions, but no reliable spectrum from the sample could be obtained due to the strong scattering from the MgO substrate. This confirms that the 20Y/BZO film is a suitable sample to explore the use and advantage of UV Raman spectroscopy with respect to visible Raman spectroscopy.

UV Raman spectroscopy measurements were performed on both samples, the polycrystalline BZO and the 500 nm film of 20Y/BZO, and for comparison also on the bare substrate material (MgO), using the custom-made UT-3 Raman spectrometer at the Center for Free Electron Laser (CFEL) Science, in Hamburg, Germany [30]. A Tsunami Ti:sapphire laser system model 3950-X1BB (Spectra Physics Lasers Inc., California), with a spectral range from 1.24 eV to 1.72 eV, was used as laser source. The fundamental laser line was frequency doubled and tripled using a flexible harmonics generation unit, model GWU2 23-PS (GWU-Lasertechnik Vertriebsges. mbH, Erfstadt, Germany), respectively, giving access to excitation energies (E_γ) between 1.55 eV and 5.17 eV (in wavelength from 800 nm to 240 nm). Raman spectra were measured under ambient conditions at the following E_γ : 5.17 eV, 4.96 eV, 4.77 eV, 4.59 eV, 4.43 eV, 4.27 eV, 4.13 eV, 3.44 eV and 2.95 eV with a spot size of 25 μm , laser powers of 7.2 mW to 27.7 mW, and acquisition times up to 600 s. The intensity was normalized to power and acquisition time and was corrected for the spectral sensitivity of the spectrometer.

3. Results and discussion

3.1. Raman spectra and peak fit analysis

The Raman spectrum as recorded on the polycrystalline BZO sample using visible light (514 nm, 2.41 eV) is shown in figure 1. The spectrum contains several features in the energy range of 150–1300 cm^{-1} , which are in full accordance with previous reports [20, 22–26, 31].

We remark that, according to x-ray and neutron diffraction investigations, BZO has a cubic perovskite structure (space group Pm-3m) [22–24, 26, 34–37], and that the Raman spectrum of a perfectly cubic perovskite is expected to be featureless [23]. It has been debated whether the presence of features in the Raman spectrum of BZO reflects the lowering of symmetry due to local distortions, indicating that the material is cubic only on average, or if the features originate from second

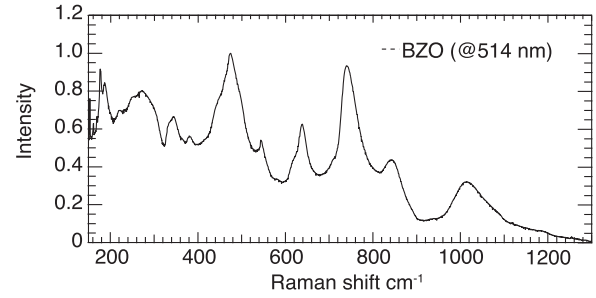


Figure 1. Raman spectrum as recorded on the polycrystalline BZO sample for excitation at 514 nm.

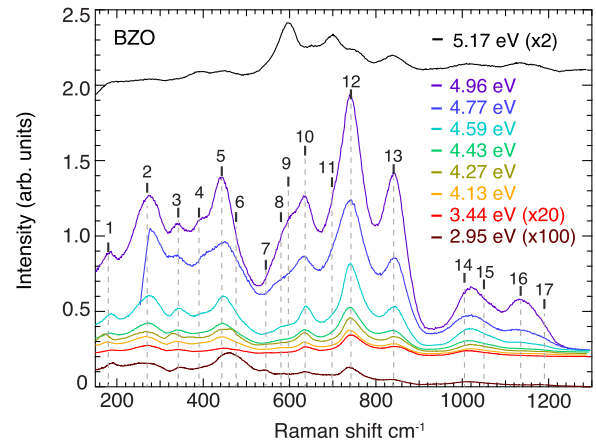


Figure 2. Raman spectra of the polycrystalline sample of BZO recorded using different E_γ . The positions of the peaks in the spectra are also shown. For an easier comparison between the spectra measured at different E_γ , the spectra are vertically shifted and some spectra are scaled according to the factors indicated in the legends.

order Raman scattering [18, 20, 23, 32, 33]. Recently, Toulouse *et al* reported on a combined Raman spectroscopy and computational study of BZO aimed to clarify the origin of the Raman spectrum of BZO [31]. It could be concluded that the observed Raman spectrum of BZO, upon excitation at 442 nm (2.8 eV), is indeed of second order [31]. Results from a recent neutron scattering and first-principles calculations study give supports for a cubic structure, and hence that the Raman features are not related to structural distortions, all the way down to $T = 0$ K [34].

Figures 2 and 3 compares the UV Raman spectra for both samples, i.e. the polycrystalline BZO and the 500 nm thick film of 20Y/BZO, as measured for different E_γ . The Raman spectra of the bare substrate material, MgO, for the same settings are shown in figure 4, and a direct comparison between the 20Y/BZO and MgO spectra is shown in figure 5. For vibrational energies higher than 800 cm^{-1} , spectral features of the MgO substrate interfere with the Raman spectrum of 20Y/BZO and, therefore this spectral region is not analyzed further here. For the lowest excitation energy ($E_\gamma = 2.95$ eV), the Raman spectra of both samples are very weak, whereas upon increasing E_γ the Raman spectra show a trend of an increasing spectral intensity. For the BZO sample, the measured spectral intensity increases by as much as

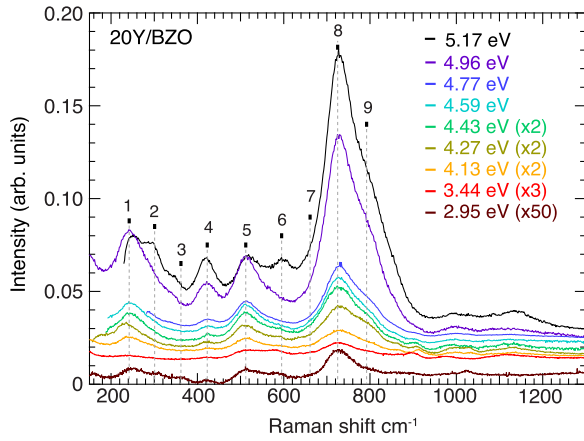


Figure 3. Raman spectra of the 20Y/BZO film recorded using different E_γ . The positions of the identified peaks in the spectra are also shown. For an easier comparison between the spectra measured at different E_γ , the spectra are vertically shifted and some spectra are scaled according to the factors indicated in the legend.

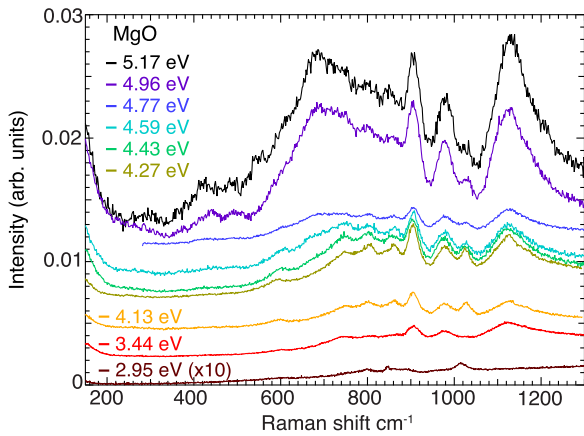


Figure 4. Raman spectra of MgO, as measured for different E_γ . The spectra are vertically shifted for easier comparison and some spectra are scaled according to the factors indicated in the legend.

≈ 500 times, and for the 20Y/BZO sample it increases by ≈ 300 times.

For BZO (figure 2), the spectra measured for $2.95 \text{ eV} \leq E_\gamma \leq 4.96 \text{ eV}$ are overall similar to each other, whereas the spectrum recorded at $E_\gamma = 5.17 \text{ eV}$ differs significantly from the others in terms of the relative intensity of the observed peaks. Further, at $E_\gamma = 5.17$ the overall spectral intensity drops considerably. This effect will be further discussed in the following, together with the intensity profiles.

As highlighted in figure 6(a), a total of 17 peaks (marked as ν_1 – ν_{17}) were identified in the wavelength region 150 – 1200 cm^{-1} . A peak fit analysis of the spectra shows that each spectrum can be adequately reproduced by 17 pseudo-Voigt components and a linearly sloping background. Figure 7(a) shows the peak fit of the Raman spectrum of BZO measured at $E_\gamma = 4.96 \text{ eV}$, as an example, whereas table 1 compiles the positions of each band. Our complete peak fit analysis for the BZO sample is shown in figure S1 (<https://stacks.iop.org/JPCM/32/405403/mmedia>).

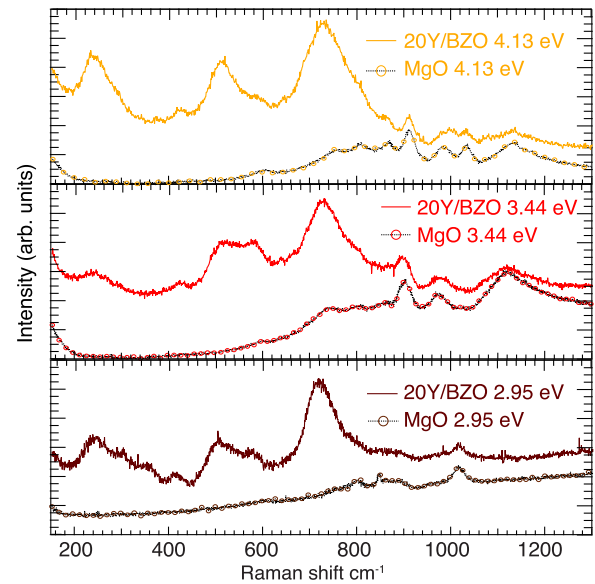


Figure 5. Raman spectra of 20Y/BZO and MgO, as measured for different E_γ . The spectra are vertically shifted for easier comparison.

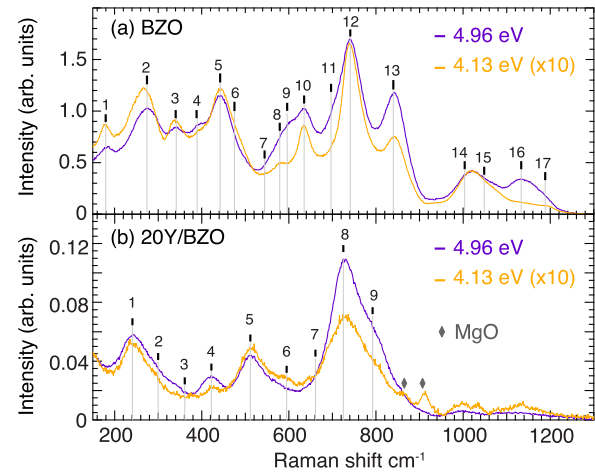


Figure 6. Comparison of the Raman spectra as measured for $E_\gamma = 4.96 \text{ eV}$ and $E_\gamma = 4.13 \text{ eV}$ (multiplied by a factor 10) on the polycrystalline BZO sample (a) and on the 20Y/BZO film (b). The positions of the identified peaks in the (a) and (b) spectra are indicated. In (b) the position of peaks belonging to the MgO substrate are also indicated.

One should note that the relative intensity of some peaks varies somewhat among the spectra, see figure 2; for instance, for $E_\gamma = 2.95 \text{ eV}$, the peak ν_7 (at 545 cm^{-1}) is more visible than in the other spectra. Additionally, the last peaks (ν_{16} – ν_{17}) are almost invisible for low E_γ , and therefore the fit of the corresponding region less reliable.

We remark that, in general, the visible and UV Raman spectra are similar to each other (figure S2) and consistent with previously published Raman spectra recorded, upon excitation at 488 and 514 nm, on samples with the same or similar compositions [18, 20, 23, 24, 31].

For 20Y/BZO (figure 3) all spectra measured are overall similar to each other and nine peaks (marked as ν'_1 – ν'_9) were identified, in each spectrum, in the wavelength region

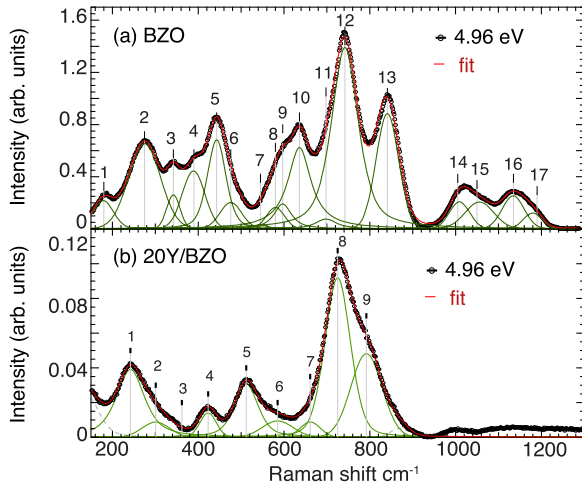


Figure 7. Raman spectra of BZO and 20Y/BZO as measured for $E_\gamma = 4.96$, together with the peak fitted components (green lines) and the total fits to the data (red line).

Table 1. Compilation of the spectral components identified at $E_\gamma = 4.96$ eV for the BZO sample.

| BZO | |
|--------------------------------|------|
| Peak position/cm ⁻¹ | |
| ν_1 | 179 |
| ν_2 | 275 |
| ν_3 | 342 |
| ν_4 | 389 |
| ν_5 | 443 |
| ν_6 | 476 |
| ν_7 | 545 |
| ν_8 | 580 |
| ν_9 | 597 |
| ν_{10} | 636 |
| ν_{11} | 698 |
| ν_{12} | 742 |
| ν_{13} | 841 |
| ν_{14} | 1009 |
| ν_{15} | 1056 |
| ν_{16} | 1134 |
| ν_{17} | 1180 |

200–800 cm⁻¹, as shown in figure 6(b). Two minor, yet visible contributions belonging to the MgO substrate could be identified in several spectra around 865 and 907 cm⁻¹, respectively.

Figure 7(b) shows the peak fit of the Raman spectrum of 20Y/BZO measured at $E_\gamma = 4.96$ eV, as an example, whereas table 2 compiles the positions of each band. Our complete peak fit analysis for the Y20/BZO sample is provided in figure S3. The wavelength region 200–800 cm⁻¹ of each spectrum was adequately reproduced by nine pseudo-Voigt components and a linearly sloping background. Note that, when necessary, the peaks belonging to the MgO substrate and an additional peak at 150 cm⁻¹ were included in the fit. Finally, for $E_\gamma = 4.77$ eV and $E_\gamma = 5.17$ eV, the fit of the spectra was possible only above 350 cm⁻¹, and therefore no data is available for the ν'_1 , ν'_2 and ν'_3 peaks. Overall, the relative intensity of

Table 2. Compilation of the spectral components identified at $E_\gamma = 4.96$ eV for the 20Y/BZO sample.

| 20Y/BZO | |
|--------------------------------|-----|
| Peak position/cm ⁻¹ | |
| ν'_1 | 241 |
| ν'_2 | 301 |
| ν'_3 | 362 |
| ν'_4 | 423 |
| ν'_5 | 512 |
| ν'_6 | 585 |
| ν'_7 | 661 |
| ν'_8 | 725 |
| ν'_9 | 792 |

the spectral components shows some, yet minor, variation. The spectra are consistent with previously published Raman spectra recorded, upon excitation at 488 and 514 nm, on samples with the same and similar compositions [18, 19, 23, 38].

3.2. Intensity profiles

For a more detailed analysis of the spectra, we focus on the evolution of the integrated intensity of each one of the Raman bands as a function of E_γ . Following the approach described in reference [30], the Raman raw data were first corrected in order to take into account the energy dependence of the optical properties of the samples, e.g. the penetration depth. More details can be found in the section S2 of supporting information. The (corrected) integrated intensity profiles for the 17 bands of the BZO Raman spectra are shown in figure 8, whereas the integrated intensity profiles for the nine bands of the 20Y/BZO Raman spectra are shown in figure 9. We observe that for all bands the data for 2.95 eV and 3.44 eV are very weak, and all bands show a clear increase of intensity as a function of increasing E_γ .

For BZO, the intensity increases as a function of increasing E_γ up to 4.96 eV, and, as noted earlier, an intensity drop is observed between 4.96 eV and 5.17 eV. As highlighted in figure 10, the spectrum recorded at $E_\gamma = 5.17$ eV shows, with respect to the other spectra, a change in the relative spectral weight of the different peaks. In particular, one can observe a clear increase of the relative intensity of the peaks ν_9 and ν_{11} , and a minor increase of relative intensity of peak ν_4 . At the same time, peaks ν_5 , ν_{10} and ν_{12} experience a loss of relative intensity.

The analysis presented above suggests the presence of two distinct characteristic energies, one around 5 eV, and one above 5 eV. The observed values are comparable with experimentally measured values of the optical bandgap, which are found in the range of 3.5–5.4 eV [22, 26, 28, 35–37, 40]. The relatively large spread in bandgap energies may be related to small variations in the defect structure of the respective samples, as defects such as oxygen and cation vacancies, may form electronic defect states within the bandgap, that may be manifested as a lowering of the actual bandgap in a measurement. Such a picture is supported by several observations of

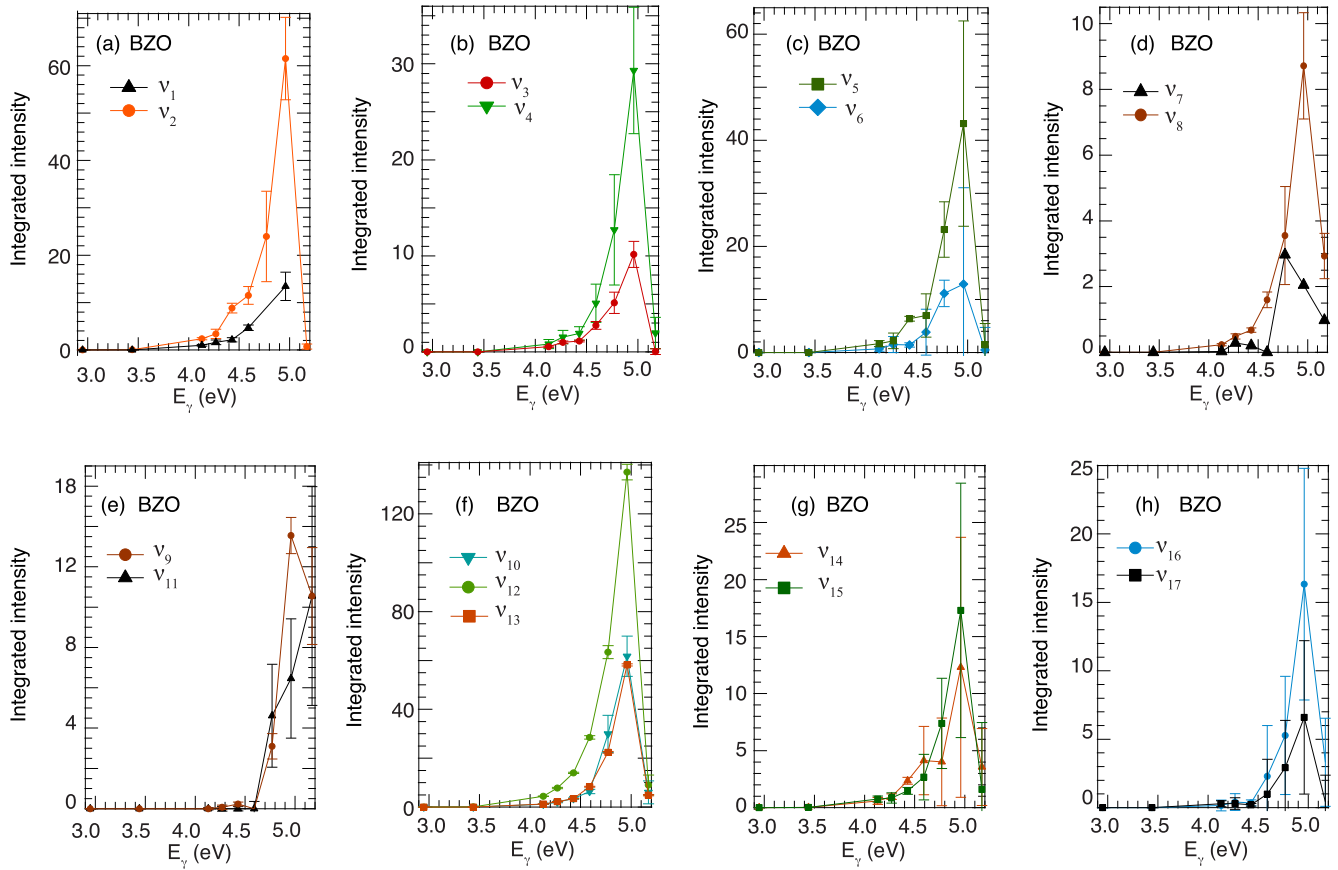


Figure 8. Integrated intensity profiles for each of the 17 peaks identified in the spectra of BZO. Error bars were calculated from the fit of the spectra.

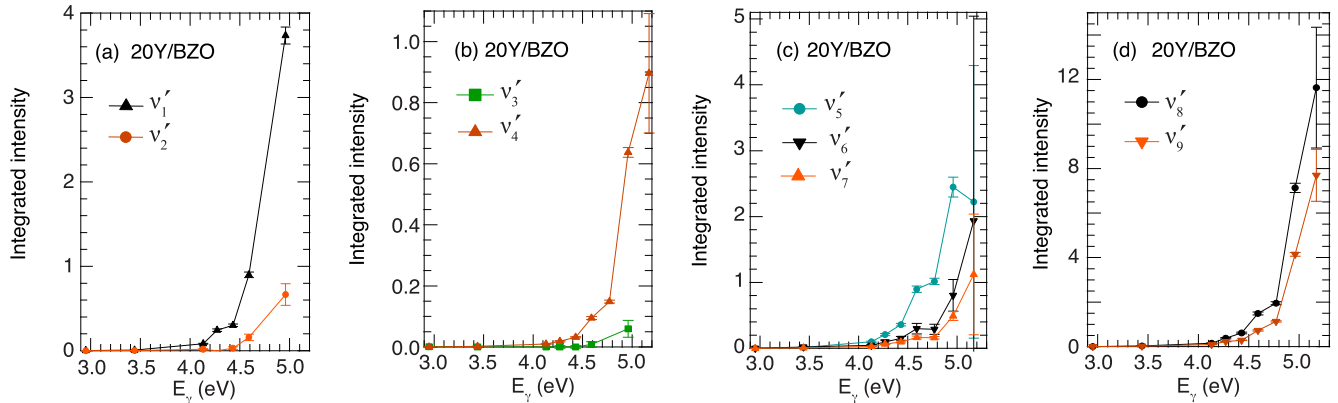


Figure 9. Integrated intensity profiles for each of the nine peaks identified in the spectra of 20Y/BZO. Error bars were calculated from the fit of the spectra.

luminescence in BZO and similar materials [22, 28, 35–37, 40, 43, 44]. Similarly, computed values of the bandgap may vary between 4.68 eV and 5.3 eV, depending on the specific method and computational details [28, 39, 41–43].

As discussed above, values in the range from 4.96 eV to 5.17 eV are comparable with expectations for the bandgap of BZO, but the exact value of the bandgap depends on the level of defects characteristic of the specific investigated sample. Therefore, it is not possible, at this stage, to assign the observed resonances to some specific electronic levels, and

a more in-depth investigation of the electronic (and phonon) structure of BZO is beyond the scope of the present work. Nevertheless, these results are very encouraging and open up for further investigations of the electronic and phononic properties of BZO. Experimentally, follow up UV Raman studies could include both polarization and temperature dependence to generate a more detailed understanding of the sample response in the UV and its relation to the band structure of the material, including the possibility of an activation of modes that are not phonon-related (e.g. plasmon or spin-wave modes).

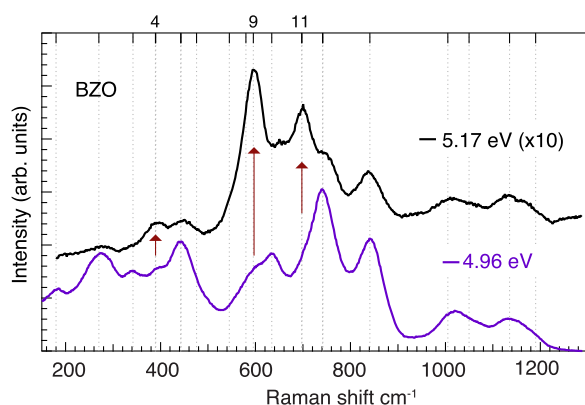


Figure 10. UV-Raman spectra as recorded for the polycrystalline BZO sample for excitation at 5.17 eV and 4.96 eV, respectively, together with the peak positions as obtained from the fit of the data. The increase of the relative spectral intensity for the peaks 4, 9 and 11, as described in the text, is highlighted in the figure.

Moving to Y2O/BZO, the intensity of all bands except ν'_5 seems to constantly increase as a function of E_γ . The ν'_5 band is featured by a maximum intensity at around 5 eV. Note that, as pointed out earlier, the data at $E_\gamma = 4.77$ eV and $E_\gamma = 5.17$ eV for the ν'_1 , ν'_2 and ν'_3 peaks are missing. The observed intensity profiles suggest the activation of a resonance effect above 5 eV, which is comparable with the values discussed above for the bandgap of BZO. In this respect, we remark that the bandgap is sensitive to the degree of structural disorder/symmetry of the perovskite lattice [22, 28, 35, 37, 40, 44]. More specifically, the introduction of acceptor dopants is expected to lead to a lowering of the bandgap [35, 37, 40]. However, considering our data, we do not have evidence to infer that 20Y/BZO is more disordered than BZO. Yet, we would like to stress that one cannot simply estimate the bandgap from the resonance energy, and, therefore, a comparison of the electronic structures based on the observed resonance behaviors is not straightforward.

By bringing together the results discussed above, we find that the vibrational spectrum of BZO is stable under UV probing for excitation energies up to 5 eV, whereas the one of 20Y/BZO is stable even at higher excitation energies. For both materials, the Raman spectral intensity is highly enhanced by the use of UV light as excitation source. In effect, this suggests that UV Raman spectroscopy may be a powerful approach for local structure studies of samples which cannot be investigated using visible Raman spectroscopy, such as BZO based oxide thin films or other materials with a weak visible Raman spectrum and/or a small sample volume. Furthermore, these results pave the way for entirely new types of studies, such as time-resolved Raman spectroscopy experiments on proton conducting perovskite materials, which can be expected to require a strong signal from thin film samples.

4. Conclusions

We have characterized the vibrational spectra of a polycrystalline sample of BaZrO₃ and a 500 nm thick film of BaZr_{1-x}Y_xO_{3-x/2} with $x = 0.20$, using visible and UV Raman

spectroscopy techniques by changing the excitation energy between 2.41 eV and 5.17 eV. Analysis of the Raman spectra reveals the activation of a strong resonance in the Raman signal when the excitation energy approaches 5 eV from below. Although the UV Raman spectra are greatly enhanced with respect to the Raman spectra measured using visible light, the number and positions of the Raman peaks are essentially the same in the visible and UV Raman spectra, suggesting that the UV Raman spectra contain all the information accessible using visible light. These results motivate the use of UV Raman spectroscopy as a powerful tool to study local structural properties of BaZrO₃ based materials and of materials featured by symmetry-forbidden vibrations in the non-resonant case, or of samples characterized by a small sample volume.

Acknowledgments

MK and LB are grateful for support from the Swedish Research Council (Grant No. 2008-6652, 2010-3519 and 2011-4887) and the Swedish Foundation for Strategic Research (Grant No. ICA10-0001). JA acknowledges support from the project Advanced research using high intensity laser produced photons and particles (ADONIS) (CZ.02.1.01/0.0/0.0/16 019/0000789) from the European Regional Development Fund, the Ministry of Education, Youth and Sports as part of targeted support from the National Programme of Sustainability II and the Chalmers Area of Advanced Materials Science. Prof. Martin Lerch, Technische Universität Berlin, is thanked for providing the polycrystalline BaZrO₃ sample.

ORCID iDs

Laura Mazzei <https://orcid.org/0000-0002-2518-709X>

Florian Biebl <https://orcid.org/0000-0002-6926-1044>

Maths Karlsson <https://orcid.org/0000-0002-2914-6332>

References

- [1] Kilner J A and Burriel M 2014 Materials for intermediate-temperature solid-oxide fuel cells *Annu. Rev. Mater. Res.* **44** 365–93
- [2] Karlsson M 2015 Proton dynamics in oxides: insight into the mechanics of proton conduction from quasielastic neutron scattering *Phys. Chem. Chem. Phys.* **17** 26–38
- [3] Björketun M E, Sundell P G, Wahnström G and Engberg D 2005 A kinetic Monte Carlo study of proton diffusion in disordered perovskite structured lattices based on first-principles calculations *Solid State Ion.* **176** 3035–40
- [4] Norby T, Widerøe M, Glöckner R and Larring Y 2004 Hydrogen in oxides *Dalton Trans.* **0** 3012–8
- [5] Björketun M E, Sundell P G and Wahnström G 2007 Effect of acceptor dopants on the proton mobility in BaZrO₃: a density functional investigation *Phys. Rev. B* **76** 054307
- [6] Samgin A 2000 Lattice-assisted proton motion in perovskite oxides *Solid State Ion.* **136–137** 291–5
- [7] Samgin A L 2013 Lattice-assisted proton hopping in oxides at low temperatures *J. Phys. Chem. Solids* **74** 1661–8

- [8] Tomoyose T, Shimoji N and Wakamura K 2005 Proton diffusion in perovskite-type oxides based on small polaron model *J. Phys. Soc. Japan* **74** 3011–5
- [9] Spahr E J, Wen L, Stavola M, Boatner L A, Feldman L C, Tolk N H and Lüpke G 2009 Proton tunneling: a decay channel of the O–H stretch mode in KTaO_3 *Phys. Rev. Lett.* **102** 075506
- [10] Spahr E J, Wen L, Stavola M, Boatner L A, Feldman L C, Tolk N H and Lüpke G 2010 Giant enhancement of hydrogen transport in rutile TiO_2 at low temperatures *Phys. Rev. Lett.* **104** 205901
- [11] Pergolesi D, Fabbri E, D'Epifanio A, Di Bartolomeo E, Tebano A, Sanna S, Licoccia S, Balestrino G and Traversa E 2010 High proton conduction in grain-boundary-free yttrium-doped barium zirconate films grown by pulsed laser deposition *Nat. Mater.* **9** 846–52
- [12] Mazzei L, Wolff M, Pergolesi D, Dura J A, Börjesson L, Gutfreund P, Bettinelli M, Lippert T and Karlsson M 2016 Structure and conductivity of epitaxial thin films of In-doped BaZrO_3 -based proton conductors *J. Phys. Chem. C* **120** 28415–22
- [13] Kim Y B, Gür T M, Jung H-J, Kang S, Sinclair R and Prinz F B 2011 Effect of crystallinity on proton conductivity in yttrium-doped barium zirconate thin films *Solid State Ion.* **198** 39–46
- [14] Fluri A, Marcolongo A, Roddatis V, Wokaun A, Pergolesi D, Marzari N and Lippert T 2017 Enhanced proton conductivity in Y-doped BaZrO_3 via strain engineering *Adv. Sci.* **4** 1700467
- [15] Higuchi T, Owaku T, Iida Y, Sakai E, Kobayashi M and Kumigashira H 2015 Proton conduction of $\text{BaCe}_{0.9}\text{Y}_{0.1}\text{O}_{3-\delta}$ thin film with lattice distortion *Solid State Ion.* **270** 1–5
- [16] Traversa E 2009 Toward the miniaturization of solid oxide fuel cells *Electrochem. Soc. Interface* **18** 49
- [17] Fabbri E, Bi L, Pergolesi D and Traversa E 2012 Towards the next generation of solid oxide fuel cells operating below 600 °C with chemically stable proton-conducting electrolytes *Adv. Mater.* **24** 195–208
- [18] Chemarin C, Rosman N, Pagnier T and Lucazeau G 2000 A high-pressure Raman study of mixed perovskites $\text{BaCe}_x\text{Zr}_{1-x}\text{O}_3$ ($0 \leq x \leq 1$) *J. Solid State Chem.* **149** 298–307
- [19] Mazzei L, Perrichon A, Mancini A, Malavasi L, Parker S F, Börjesson L and Karlsson M 2019 Local coordination of protons in In- and Sc-doped BaZrO_3 *J. Phys. Chem. C* **123** 26065–72
- [20] Karlsson M, Ahmed I, Matic A and Eriksson S-G 2010 Short-range structure of proton-conducting $\text{BaM}_{0.10}\text{Zr}_{0.90}\text{O}_{2.95}$ ($\text{M} = \text{Y, In, Sc and Ga}$) investigated with vibrational spectroscopy *Solid State Ion.* **181** 126–9
- [21] Mazzei L, Perrichon A, Mancini A, Wahnström G, Malavasi L, Parker S F, Börjesson L and Karlsson M 2019 Local structure and vibrational dynamics in indium-doped barium zirconate *J. Mater. Chem. A* **7** 7360–72
- [22] Aguiar E C, Simões A Z, Paskocimas C A, Cilense M, Longo E and Varela J A 2015 Photoluminescence of BaZrO_3 explained by a order/disordered transformation *J. Mater. Sci., Mater. Electron.* **26** 1993–2001
- [23] Karlsson M, Matic A, Knee C S, Ahmed I, Eriksson S G and Börjesson L 2008 Short-range structure of proton-conducting perovskite $\text{BaIn}_x\text{Zr}_{1-x}\text{O}_{3-x/2}$ ($x = 0-0.75$) *Chem. Mater.* **20** 3480–6
- [24] Shi F, Dong H, Liu Q, Yang J, Ren S, Sun H and Xiong J 2016 Investigation and theoretical calculation of the lattice vibrational spectra of BaZrO_3 ceramic *J. Mater. Sci., Mater. Electron.* **28** 3467–73
- [25] Chen Q et al 2011 Effect of compressive strain on the Raman modes of the dry and hydrated $\text{BaCe}_{0.8}\text{Y}_{0.2}\text{O}_3$ proton conductor *J. Phys. Chem. C* **115** 24021–7
- [26] Xin C et al 2019 Single crystal growth of BaZrO_3 from the melt at 2700 °C using optical floating zone technique and growth prospects from BaB_2O_4 flux at 1350 °C *CrystEngComm* **21** 502–12
- [27] Łupina G et al 2009 Dielectric constant and leakage of BaZrO_3 films *Appl. Phys. Lett.* **94** 152903
- [28] Cavalcante L S et al 2008 Experimental and theoretical correlation of very intense visible green photoluminescence in powders *J. Appl. Phys.* **103** 63527
- [29] Paun M S 2015 *Single crystal growth of high melting oxide materials by means of induction skull melting (PhD Thesis)* Berlin: Technische Universität Berlin DOI: [10.14279/depositonce-4796](https://doi.org/10.14279/depositonce-4796)
- [30] Schulz B, Bäckström J, Budelmann D, Maeser R, Rübhausen M, Klein M V, Schoeffel E, Mihill A and Yoon S 2005 Fully reflective deep ultraviolet to near infrared spectrometer and entrance optics for resonance Raman spectroscopy *Rev. Sci. Instrum.* **76** 073107
- [31] Toulouse C et al 2019 Lattice dynamics and Raman spectrum of BaZrO_3 single crystals *Phys. Rev. B* **100** 134102
- [32] Bilić A and Gale J D 2009 Ground state structure of BaZrO_3 : a comparative first-principles study *Phys. Rev. B* **79** 174107
- [33] Lebedev A I and Sluchinskaya I A 2015 Combined first-principles and EXAFS study of structural instability in BaZrO_3 *J. Adv. Dielectr.* **05** 1550019
- [34] Perrichon A, Jedvik Granhed E, Romanelli G, Piovano A, Lindman A, Hyldgaard P, Wahnström G and Karlsson M 2020 Unraveling the ground-state structure of BaZrO_3 by neutron scattering experiments and first-principles calculations *Chem. Mater.* **32** 2824–35
- [35] Butt S H, Rafique M S, Bashir S, Ilyas U, Siraj K, Awan M S, Mehmood K, Rafique M and Afzal A 2017 Influence of Er doping on the structural, optical and luminescence properties of pulsed laser deposited Er: BaZrO_3 thin films *Ceram. Int.* **43** 12162–6
- [36] Parida S et al 2012 Structural refinement, optical and microwave dielectric properties of BaZrO_3 *Ceram. Int.* **38** 2129–38
- [37] Satapathy A and Sinha E 2018 Optical band gap and photoluminescence studies of samarium-doped barium zirconate perovskite prepared by solid state reaction route *J. Appl. Spectrosc.* **84** 948–53
- [38] Karlsson M, Matic A, Zanghellini E and Ahmed I 2010 Temperature-dependent infrared spectroscopy of proton-conducting hydrated perovskite $\text{BaIn}_x\text{Zr}_{1-x}\text{O}_{3-x/2}$ ($x = 0.10-0.75$) *J. Phys. Chem. C* **114** 6177–81
- [39] Linderälv C, Lindman A and Erhart P 2018 A unifying perspective on oxygen vacancies in wide band gap oxides *J. Phys. Chem. Lett.* **9** 222–8
- [40] Borja-Urby R, Diaz-Torres L A A, Salas P, Vega-Gonzalez M and Angeles-Chavez C 2010 Blue and red emission in wide band gap BaZrO_3 : Yb^{3+} , Tm^{3+} *Mater. Sci. Eng. B* **174** 169–73
- [41] Bjørheim T S, Arrigoni M, Gryaznov D, Kotomin E and Maier J 2015 Thermodynamic properties of neutral and charged oxygen vacancies in BaZrO_3 based on first principles phonon calculations *Phys. Chem. Chem. Phys.* **17** 20765–74
- [42] Lindman A, Erhart P and Wahnström G 2015 Implications of the band gap problem on oxidation and hydration in acceptor-doped barium zirconate *Phys. Rev. B* **91** 245114
- [43] Gurgel M F C, Moreira M L, Paris E C, Espinosa J W M, Pizani P S, Varela J A and Longo E 2011 BaZrO_3 photoluminescence property: an *ab initio* analysis of structural deformation and symmetry changes *Int. J. Quantum Chem.* **111** 694–701
- [44] Moreira M L et al 2008 Photoluminescence of barium titanate and barium zirconate in multilayer disordered thin films at room temperature *J. Phys. Chem. A* **112** 8938–42